12-24-2013

Assessment of Water Droplet Evaporation Mechanisms on Hydrophobic and Superhydrophobic Substrates

Zhenhai Pan
Purdue University, panzhh@purdue.edu

Susmita Dash
Purdue University, Birck Nanotechnology Center, sdash@purdue.edu

Justin A. Weibel
Purdue University, Birck Nanotechnology Center, jaweibel@purdue.edu

Suresh V. Garimella
Birck Nanotechnology Center and Cooling Technologies Research Center, Purdue University, sureshg@purdue.edu

Pan, Zhenhai; Dash, Susmita; Weibel, Justin A.; and Garimella, Suresh V., "Assessment of Water Droplet Evaporation Mechanisms on Hydrophobic and Superhydrophobic Substrates" (2013). *Birck and NCN Publications.* Paper 1537.
http://dx.doi.org/10.1021/la4045286

Langmuir

Article

pubs.acs.org/Langmuir

Assessment of Water Droplet Evaporation Mechanisms on Hydrophobic and Superhydrophobic Substrates

Zhenhai Pan, Susmita Dash, Justin A. Weibel, and Suresh V. Garimella*

School of Mechanical Engineering and Birck Nanotechnology Center, Purdue University, 585 Purdue Mall, West Lafayette, Indiana 47907, United States

ABSTRACT: Evaporation rates are predicted and important transport mechanisms identified for evaporation of water droplets on hydrophobic (contact angle ~110°) and superhydrophobic (contact angle ~160°) substrates. Analytical models for droplet evaporation in the literature are usually simplified to include only vapor diffusion in the gas domain, and the system is assumed to be isothermal. In the comprehensive model developed in this study, evaporative cooling of the interface is accounted for, and vapor concentration is coupled to local temperature at the interface. Conjugate heat and mass transfer are solved in the solid substrate, liquid droplet, and surrounding gas. Buoyancy-driven convective flows in the droplet and vapor domains are also simulated. The influences of evaporative cooling and convection on the evaporation characteristics are determined quantitatively. The liquid−vapor interface temperature drop induced by evaporative cooling suppresses evaporation, while gas-phase natural convection acts to enhance evaporation. While the effects of these competing transport mechanisms are observed to counterbalance for evaporation on a hydrophobic surface, the stronger influence of evaporative cooling on a superhydrophobic surface accounts for an overprediction of experimental evaporation rates by ~20% with vapor diffusion-based models. The local evaporation fluxes along the liquid−vapor interface for both hydrophobic and superhydrophobic substrates are investigated. The highest local evaporation flux occurs at the three-phase contact line region due to proximity to the higher temperature substrate, rather than at the relatively colder droplet top; vapor diffusion-based models predict the opposite. The numerically calculated evaporation rates agree with experimental results to within 2% for superhydrophobic substrates and 3% for hydrophobic substrates. The large deviations between past analytical models and the experimental data are therefore reconciled with the comprehensive model developed here.

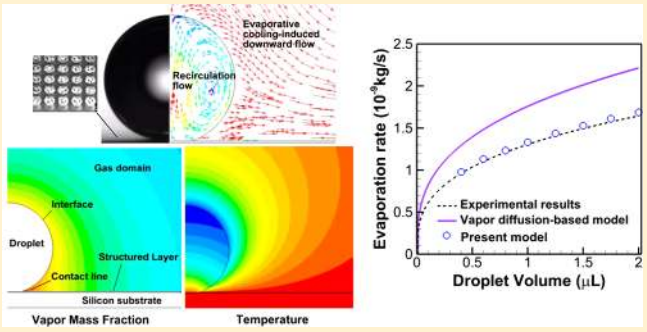

1. INTRODUCTION

Evaporation of sessile droplets on a solid substrate is an important fundamental phenomenon in various applications including phase-change cooling,[1,2] inkjet printing,[3,4] controlled deposition of self-assembled surface coatings,[5,6] and microfluidic lab-on-a-chip processes,[7,8] to name a few. A comprehensive understanding of the underlying physical mechanisms is critically important in utilizing droplet evaporation-based processes in such applications.

Picknett and Bexon[9] were among the first researchers to study evaporation of a sessile droplet in ambient air and suggested that two droplet evaporation modes exist on a smooth substrate: a constant contact radius (CCR) mode in which the contact radius remains fixed while the contact angle reduces and a constant contact angle (CCA) mode in which the contact angle remains constant while the contact radius recedes due to evaporation. Assuming that vapor diffusion in the surrounding air was the only factor influencing evaporation rate, they derived a theoretical solution for the evaporation rate from the governing diffusion equations. Bourges-Monnier and Shanahan[10] studied evaporating droplets of water and *n*-decane on various substrates that provided a range of initial droplet contact angles. A simplified expression for evaporation in the CCR mode was proposed as an approximation to previous vapor diffusion-based models;[9] the expression was in good agreement with the full analytical solution of the vapor diffusion model when the contact angle was near 90°.[11] Hu and Larson[12] studied vapor diffusion from evaporating droplets experimentally, analytically, and numerically using a finite-element method. The results were reduced to a simple expression for the total evaporation rate under the approximation of a wetting contact angle (<90°). Popov[13] derived vapor diffusion-based solutions for both the total evaporation rate and local interfacial evaporation flux, which could be employed for a droplet with any arbitrary contact angle. Vapor diffusion-based models are widely employed to predict droplet evaporation characteristics.[14−18]

Droplet evaporation involves a number of other complex transport mechanisms, in addition to vapor diffusion in the gas domain. For instance, the droplet interface is cooled during evaporation due to the latent heat of absorption during phase change from liquid to vapor. Cooling of the droplet interface

Received: September 10, 2013
Revised: December 2, 2013
Published: December 9, 2013

   dx.doi.org/10.1021/la4045286 | *Langmuir* 2013, 29, 15831−15841

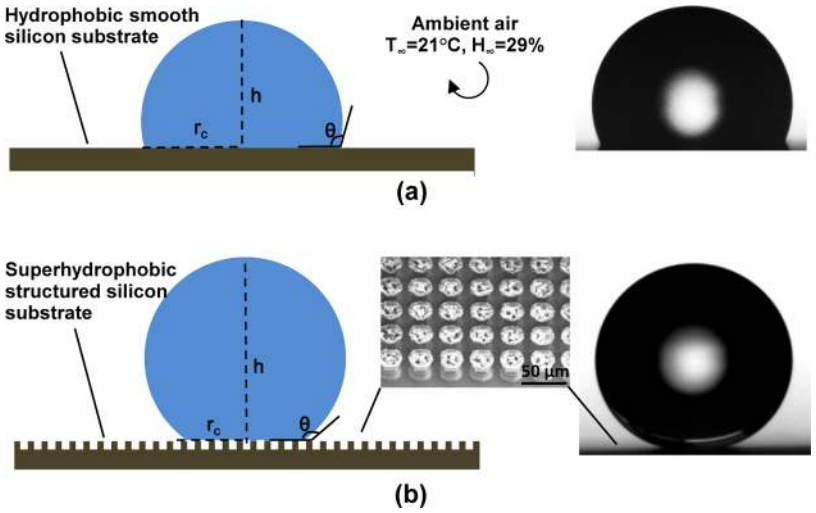

Figure 1. Schematic illustrations (left) and images obtained from experiments[49] (right) of a droplet evaporating on (a) a smooth hydrophobic substrate (θ = 110°) and (b) a structured superhydrophobic substrate (θ = 160°). The inset shows an SEM image of the superhydrophobic surface used in the experiments.[49]

induces temperature gradients that drive heat transfer in the solid, liquid, and gas phases. Experimental evidence of such evaporative cooling of the liquid−gas interface was provided by David et al.,[19] specifically during intense evaporation or on low-conductivity substrates. Dunn et al.[20] improved previous vapor diffusion-based models by including the evaporative cooling effect as well as thermal conduction in the droplet and underlying solid substrate. The predicted evaporation rates of organic fluid droplets were consistent with experiments, while previous vapor diffusion-based models overestimated the evaporation rates. Saada et al.[21] further improved upon the model of Dunn et al.[20] by accounting for thermal diffusion in the gas domain. As thermal conductivity of the substrate decreased, the evaporation lifetime increased significantly; this is consistent with other studies.[20,22,23] Additional factors not considered are buoyancy-driven flows and convective heat transfer from substrate to gas.

The nonuniform evaporative flux, temperature, and vapor fraction along the interface of an evaporating droplet induce convection in both liquid and gas domains. Deegan et al.[24] modeled the flow inside a droplet induced by the nonuniform evaporation. The flow pattern resulted in deposition of dispersed solids in the droplet at the contact line, forming a ring-shaped deposit per the so-called "coffee ring" effect. Subsequently, Hu and Larson[25,26] theoretically and experimentally studied Marangoni flow in both organic liquid and water droplets. Ristenpart et al.[27] and Xu et al.[28] investigated the dependence of the direction of Marangoni flow on solid substrate conductivity and droplet contact angle. Bhardwaj et al.[29] developed a comprehensive numerical model to investigate Marangoni convection in nanoliter droplets and its influence on particle deposition. Both evaporative cooling and vapor diffusion were taken into account, while natural convection in the gas domain was neglected on account of the extremely small scale of the droplet. The calculated evaporation rate and flow field agreed well with experiments. Karapetsas et al.[30] numerically investigated the hydrothermal instabilities in droplets evaporating on a heated substrate. Consistent with the experiments,[31] various patterns of temperature perturbations were presented for organic droplets. While strong Marangoni flow (velocities >1 mm/s) is usually observed in organic liquids,[26,30−32] the observed Marangoni flow in water droplets is comparatively weak (∼10 μm/s)[5,26,33] and does not influence the total evaporation rate.[34]

Compared with convection in the liquid phase of an evaporating droplet, relatively less attention has been paid to the natural convection in the surrounding gas phase. Gas-phase convection is usually more important for water droplets[20] (due to the large density difference between water vapor and air) and heated substrates.[35,36] Saada et al.[37] numerically investigated the importance of gas-phase natural convection for both heated and unheated substrates. A diffusion model was found to underestimate the evaporation rate by up to ∼27.3% for heated substrates and ∼8.5% for unheated substrates. Kelly-Zion et al.[38] proposed a semiempirical correlation that included the effects of natural convection by including a correction factor such that the vapor diffusion model[12] matched their experiments. Recently, Carle et al.[39] conducted a series of experiments which experimentally demonstrated the importance of gas-phase natural convection in droplet evaporation on heated surfaces. The vapor diffusion-based model underestimated the evaporation rate by up to 29.7% compared to their experimental results.[40] Very recently, Kelly-Zion et al.[41] provided experimental evidence at room temperature that natural convection in the gas domain influences the vapor transport and thus the evaporation process.

In the past decade, the study of droplet evaporation on superhydrophobic surfaces has attracted significant attention due to important applications such as water-proof clothing[42] and high-sensitivity molecular detection.[43,44] McHale et al.[45] and Dash et al.[46] reported that droplet evaporation on superhydrophobic substrates follows three distinct modes: the constant contact radius (CCR), constant contact angle (CCA), and mixed modes. Shin et al.[47] experimentally compared droplets evaporating on hydrophilic, hydrophobic, and superhydrophobic substrates and found that the evaporation rate and the pinning time decreased as the substrate became more hydrophobic. Gelderblom et al.[48] experimentally investigated CCR-mode water droplet evaporation on a superhydrophobic carbon nanofiber substrate at room temperature. The evaporation rates agreed well with Popov's vapor diffusion-based model.[13] Recently, Sobac and Brutin[39] experimentally

dx.doi.org/10.1021/la4045286 | Langmuir 2013, 29, 15831−15841

studied water droplet evaporation on both hydrophobic and hydrophilic substrates. It was found that the vapor diffusion-based model produced large deviations in predicting the evaporation rates for both hydrophobic and hydrophilic surfaces at elevated substrate temperatures. Dash and Garimella[49] investigated the evaporation of water droplets on both smooth hydrophobic and structured superhydrophobic substrates under ambient conditions. The experimental evaporation rates were ~20% smaller than the predicted values based on the vapor diffusion-based model[13] for the superhydrophobic substrate.

Evaporation of a sessile droplet is a complex process governed by transport mechanisms that include vapor diffusion, evaporative cooling, conjugate heat transfer, and fluid convection induced by buoyancy or by other means. While many past investigations have targeted the understanding of specific droplet evaporation processes, to the authors' knowledge, none have considered all the above factors in concert. The details of transport are therefore still not fully understood, especially for water droplet evaporation on hydrophobic and superhydrophobic substrates. In the present study, a comprehensive numerical model is developed that accounts for all of the above transport mechanisms. The numerical modeling approach is first validated against analytical vapor diffusion-based models and then used to analyze details of the transport processes in water droplets evaporating on hydrophobic and superhydrophobic substrates. By resolving the individual effects of each physical transport mechanism on evaporation in a comprehensive framework, the current model is able to assess the importance of all mechanisms at play. The critical influences of evaporative cooling and gas-phase convection on the evaporation process are identified, and their contributions to the overall evaporation rates and local evaporation fluxes are quantitatively determined.

2. PROBLEM DESCRIPTION

The simulations consider a water droplet of 2 μL initial volume evaporating from hydrophobic and superhydrophobic substrates (Figure 1). The ambient temperature and relative humidity are set at 21 °C and 29%, respectively. The droplet shapes, range of liquid−solid contact angles, substrate geometry, and ambient conditions are chosen to allow direct comparison with experimental results recently obtained in the authors' group.[49]

In the experimental study,[49] hierarchical superhydrophobic surfaces were fabricated using a single deep reactive ion etching (DRIE) step. Silicon pillars constitute the larger roughness element (height of pillars ~18 μm). During the DRIE process, a partially cured photoresist layer from a previous masking step was deformed and retained at the top of the silicon pillars to form the second-tier, hierarchical roughness (thickness of photoresist ~5 μm). The surface was then spin-coated with 0.2% solution of Teflon-AF 1600 (DuPont, Wilmington, DE) in FC-77 to render it superhydrophobic. The thickness of the Teflon layer was measured to be ~50 nm. Silicon wafers coated with the Teflon solution serve as the smooth hydrophobic surface used in the experiments. To model the hierarchical roughness elements on the superhydrophobic substrate in the numerical simulation, an additional solid layer is employed between the silicon substrate and droplet (termed the "structured layer" in Figure 1b).

The superhydrophobic surface offers a high contact angle (160°) and negligible contact angle hysteresis (<1°) for water droplets, resulting in a CCA mode of evaporation taking place at the initial contact angle.[49] The initial contact angle of the droplet on the hydrophobic substrate was ~118 ± 2°; evaporation on this surface initially occurs in a CCR mode until the contact angle decreases to ~110°, after which a CCA mode is followed. For both surfaces, the final stages of evaporation (approximately the last 10% of the total evaporation time) occurred in a mixed mode where both contact angle and contact radius decreased simultaneously. The droplet contact angle considered in the numerical model for both surfaces is the value during the predominant CCA mode of evaporation.

3. NUMERICAL MODEL

A 2D axisymmetric model is developed to describe the heat and mass transport within and surrounding the evaporating droplets shown in Figure 1. Transport mechanisms considered in the current numerical model include: thermal conduction in the solid substrate, conduction and natural convection in the liquid droplet, and heat and mass transfer in the surrounding gas domain. Evaporative cooling due to the latent heat of evaporation is accounted for, and the saturated vapor concentration is coupled to local interface temperature. Since the time scale of volume change by evaporation is significantly larger than all other transport process time scales (vapor, thermal, and momentum diffusion), a quasi-steady assumption for each droplet shape and volume during the evaporation process is appropriate[20,21] and is employed in the present model. Under this assumption, the evaporation behavior depends only on the instantaneous droplet geometry and environment conditions. Schematic diagrams of the numerical solution domains and boundary conditions are provided in Figure 2 and described below.

3.1. Liquid (Droplet) Domain. Considering the small length scale of the droplet, laminar flow of a Newtonian fluid and the Boussinesq approximation (for implementation of buoyancy-induced convection) are assumed in the liquid domain. The continuity, momentum, and energy equations, and the Boussinesq approximation, are given respectively as

$$\rho_l \nabla \cdot \vec{V} = S_{m,l} \tag{1}$$

$$\rho_l \vec{V} \cdot \nabla \vec{V} = -\nabla p + \mu_l \nabla^2 \vec{V} + \rho_{\mathrm{Bous}} \vec{g} \tag{2}$$

$$\rho_l c_{p,l} \vec{V} \cdot \nabla T = k_l \nabla^2 T + S_{h,l} \tag{3}$$

$$\rho_{\mathrm{Bous}} = \rho_{\mathrm{ref}} + \rho_{\mathrm{ref}} \beta (T - T_{\mathrm{ref}}) \tag{4}$$

where S (see Table 1 for full nomenclature) indicates the source terms employed to model heat and mass transport across the interface, as described in section 3.4.

3.2. Gas Domain. Since vapor transport in the gas domain influences the evaporation process, the flow, temperature, and concentration fields should be calculated together. In the present model, flow in the gas domain is assumed to be laminar and Newtonian. The continuity, momentum, and energy equations are given by eqs 1−3 when evaluated using gas properties (the Boussinesq term is replaced by $\rho_g \vec{g}$). The air−vapor mixture in the gas domain should follow the ideal gas law, and thus the density is given by

$$\rho_g = C_v M_v + \left(\frac{p_{\mathrm{atm}}}{RT} - C_v \right) M_{\mathrm{air}} \tag{5}$$

dx.doi.org/10.1021/la4045286 | Langmuir 2013, 29, 15831−15841

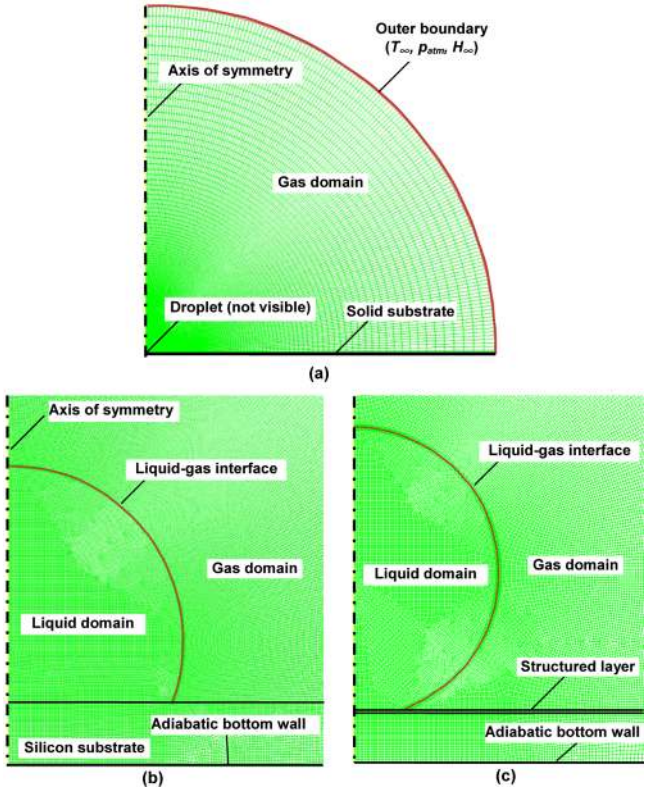

Figure 2. Schematic diagram of the numerical solution domains and boundary conditions (with mesh overlay). Shown are the (a) full domain along with details near the droplet on a (b) hydrophobic and (c) superhydrophobic substrate.

Table 1. Nomenclature

variable	description	variable	description
A	area (m^2)	p	pressure (N/m^2)
C	vapor molar conc (mol/m^3)	r	radius (m)
c_p	heat capacity (J/(kg K))	R	universal gas constant (J/(mol K))
D	diffusion coeff in air (m^2 /s)	S_m	mass source ($kg/(m^3$ s))
H	relative humidity	S_h	energy source (W/m^3)
h	height of the droplet (m)	T	temperature (K)
h_{fg}	latent heat of evaporation (J/kg)	V	fluid velocity (m/s)
h_s	sensible enthalpy (J/kg)	q	heat flux (W/m^2)
k	thermal conductivity (W/(m K))	α	thermal diffusivity (m^2/s)
l	length (m)	β	thermal expansion coeff (1/K)
M	molecular weight (kg/mol)	θ	contact angle
m''_{net}	mass flux ($kg/(m^2$ s))	μ	dynamic viscosity (N s/m^2)
$\vec{n}$	unit normal vector	ρ	density (kg/m^3)
g	gravity (m/s^2)	σ	surface tension (N/m)
subscript	description	subscript	description
1	phase 1	g	gas (vapor/air mixture)
2	phase 2	l	liquid
∞	ambient	lv	liquid−gas interface
atm	atmospheric pressure	n	component along $\vec{n}$ direction
Bous	Boussinesq	ref	reference
c	contact	v	vapor
eff	effective	sat	saturated

The governing equation for vapor diffusion and convection in air is given as

$$\vec{V}\cdot\nabla C_v - \nabla\cdot(D\cdot\nabla C_v) = 0 \tag{6}$$

Lastly, the temperature-dependent diffusion coefficient D is given by

$$D(T) = D_{ref}\left(\frac{T}{T_{ref}}\right)^{1.5} \tag{7}$$

3.3. Solid Domain. In the solid domain, thermal diffusion is governed by

$$\nabla\cdot(k\cdot\nabla T) = 0 \tag{8}$$

For the hierarchical superhydrophobic substrate, the solid domain is divided into two regions as depicted in Figure 2c. For the underlying solid silicon wafer, the thermal conductivity is straightforward, with k = 149 W/(m K). The structured layer is assumed to have a small thickness equivalent to the surface pillar height (23 μm in Dash and Garimella[49]). Because of the series arrangement of silicon pillars and air gaps, lateral thermal conduction (perpendicular to the axis of symmetry) is assumed negligible. Normal to the surface, the effective thermal conductivity is calculated as a parallel arrangement of silicon pillars (the air gaps with $k \sim 0$ are assumed to have no contribution) as

$$k_{eff} = \frac{l_{Si} + l_{ph}}{l_{Si}/k_{Si} + l_{ph}/k_{ph}}\frac{A_{pillar}}{A_{total}} \tag{9}$$

The contribution of the Teflon layer is neglected due to its very small thickness of ∼50 nm.[49] The l_{Si} and l_{ph} are the in-series heights of the silicon and photoresist portions of each pillar (l_{Si}/l_{ph} = 3.6, A_{pillar}/A_{total} = 0.473, $k_{ph} \sim$ 0.25 W/(m K)). The effective thermal conductivity of the structured layer in the surface normal direction is then obtained as k_{eff} = 0.54 W/(m K).

3.4. Liquid−Gas Interface. The vapor pressure at the interface is assumed to be the saturation value by ignoring interfacial evaporation resistance and capillary pressure drop across the interface. The interfacial resistance is usually much smaller than diffusion resistance when water is evaporating in an air ambient,[50] while the capillary pressure drop needs to be considered only for droplets with radius smaller than ∼1 μm.[51] The saturation pressure $p_{sat}(T_{lv})$ is calculated by the Clausius−Clapeyron equation:

$$p_{sat}(T_{lv}) = p_{sat\_ref}\exp\left(\frac{Mh_{fg}}{R}\left(\frac{1}{T_{sat\_ref}} - \frac{1}{T_{lv}}\right)\right) \tag{10}$$

The evaporation flux should be equal to the vapor transport at the liquid−gas interface

$$m'' = M(-D\vec{n}\cdot\nabla C_v + v_n C_v) \tag{11}$$

The first term on the right-hand side of the equation is the vapor transport due to mass diffusion, and the second term represents mass convection by Stefan flow. Since the velocity of vapor flow is roughly 3 orders of magnitude larger than the displacement velocity of the droplet interface (based on the phase density difference), displacement of the interface is neglected in eq 11. As vapor diffuses into the air, the convection represented by v_n ensures that net mass transport of air is zero. Therefore, at the interface, we have

dx.doi.org/10.1021/la4045286 | Langmuir 2013, 29, 15831−15841

$$v_n|_{lv} = -\frac{1}{C_g - C_v} D(\vec{n}\cdot\nabla C_v) \tag{12}$$

Coupling eq 11 with eq 12, we have

$$m'' = -\frac{MD}{1 - C_v/C_g}(\vec{n}\cdot\nabla C_v)|_{lv} \tag{13}$$

On the basis of the ideal-gas law, we have

$$C_g|_{lv} = \frac{p_{atm}}{RT_{lv}}, \quad C_v|_{lv} = \frac{p_{sat}(T_{lv})}{RT_{lv}} \tag{14}$$

To model the mass transport across the interface, corresponding mass sources are added to the mesh cells adjacent to either side of the interface, as explained in refs 52 and 53

$$S_{m,g} = \frac{m'' A_{cell}}{V_{cell,g}}, \quad S_{m,l} = -\frac{m'' A_{cell}}{V_{cell,l}} \tag{15}$$

where A_{cell} is the interface area of a specified cell adjacent to the interface and V_{cell} is the cell volume.

Evaporation from the interface also induces an evaporative cooling effect. This cooling effect is taken into account by employing energy sources in the mesh cells adjacent to the interface on either side:

$$S_{h,g} = S_{m,g} h_s(T), \quad S_{h,l} = S_{m,l} h_s(T) + h_{fg} S_{m,l} \tag{16}$$

$$h_s(T) = c_p(T - T_{ref,sim}) \tag{17}$$

The first terms on the right-hand sides in eq 16 represent the sensible heat contributed by the mass source, while an additional term in the liquid-phase source accounts for the latent heat absorbed during evaporation. $T_{ref,sim}$ in eq 17 is an arbitrary reference temperature implemented in the numerical simulation (section 4).

The presence of Marangoni flow in pure water at room temperature has been a subject of debate. As discussed by Hu and Larson,[25,26] the theoretically calculated Marangoni flow is over 100 times stronger than the flow observed in experiments. The authors attributed this discrepancy to the sensitivity of water to surface contamination and demonstrated that the Marangoni strength was reduced by 100 times at surfactant contaminant concentrations as small as 300 molecules/μm^2. Subsequent experiments also showed that Marangoni flow in pure water droplets at room temperature does not exist or at least is very weak (<~10 μm/s).[5,33,54] In other numerical investigations where much stronger Marangoni convection is employed, the influence on the evaporation rate was found to be weak[34] or only important for much smaller droplets (<~1 nL).[51] Therefore, in the present model, the Marangoni effect is not included considering the uncertainty in the literature over its magnitude for pure water and as is consistent with past studies.[20,21,26,33,54] The shear stress along both sides of the interface is set as zero.

3.5. Other Boundary Conditions. *Outer Gas and Solid Domain Boundary.* A notional hemispherical simulation boundary is employed for the gas domain as shown in Figure 2a. The distance from the droplet to the outer boundary is 200 times larger than the droplet radius; the evaporation rate was confirmed to be independent of the boundary location for this domain size. At the outer boundary

$$C_v = \frac{Hp_{sat}(T)}{RT} \tag{18}$$

where the ambient conditions are applied (H_∞ = 29%, T_∞ = 21 °C).

The bottom of the silicon substrate is assumed to be adiabatic as in the experiments. There is little effect on the evaporation rate (<1%) if a constant temperature boundary is applied with T = 21 °C.

Interior Boundary Conditions. The temperature across the inner interfaces is assumed to be continuous. Therefore, at all the solid−solid and fluid−solid interfaces

$$T_1 = T_2, \quad k_1(\vec{n}_1\cdot\nabla T_1) = k_2(\vec{n}_2\cdot\nabla T_2) \tag{19}$$

No-slip and no-penetration boundary conditions are employed at the fluid−solid interfaces. On the gas−liquid interface, the boundary condition is set as no shear stress (free-slip).

4. NUMERICAL SOLUTION PROCEDURE

The numerical solution is obtained using the pressure-based finite volume scheme as described in ref 55. The software package ANSYS 12.0 (FLUENT solver)[56] is employed with embedded user-defined functions where necessary. Pressure−velocity coupling is accomplished through the SIMPLE algorithm. When evaluating the sensible heat, a reference temperature $T_{ref,sim}$ is employed as a scale; i.e., the sensible heat associated with a mass flow is calculated as

$$q_s(T) = m'' c_p(T - T_{ref,sim}) \tag{20}$$

The default $T_{ref,sim}$ of 298.15 K is used in FLUENT.[56] The fluid properties used for the simulations are shown in Table 2.

Table 2. Fluid Properties

properties	water	gas
density (kg/m^3)	998.08 at 294.15 K	eq 5
thermal conductivity (W/(m K))	0.6	0.0242
thermal capacity (J/kg)	4182	1006.43
viscosity (kg/(m s))	$0.00834 - 2.5 \times 10^{-5}T$	1.789×10^{-5}
vapor molecular weight (kg/mol)	0.018	0.029 for air
thermal expansion coeff ($1/K$)	0.000251	
diffusion coeff (m^2/s)	2.54×10^{-5} at 293.65 K	
saturated vapor pressure (Pa)	2338 at 293.15 K	
latent heat (J/kg)	$2.7554 \times 10^6 - 3.46T^2$	

The mesh is shown in Figure 2. A total of ~81 000 to ~108 000 quadrilateral cells were used across all domains based on the different contact angles. A local refinement of the mesh is applied at the liquid−gas interface. To accurately capture the flow field, a total of ~12 000 cells are employed in the droplet for the hydrophobic substrate and ~14 000 cells in the droplet for the hydrophobic substrate. The mesh cells in the gas are much finer near the interface than at the outer boundary. A mesh-independence check was performed to confirm that the simulation results are insensitive to further refinement of the mesh. The changes in the evaporation rate, distribution of evaporation flux, interfacial temperature, and flow field near the droplet are all less than 0.5% for a mesh with more than twice as many cells for each case.

dx.doi.org/10.1021/la4045286 | Langmuir 2013, 29, 15831−15841

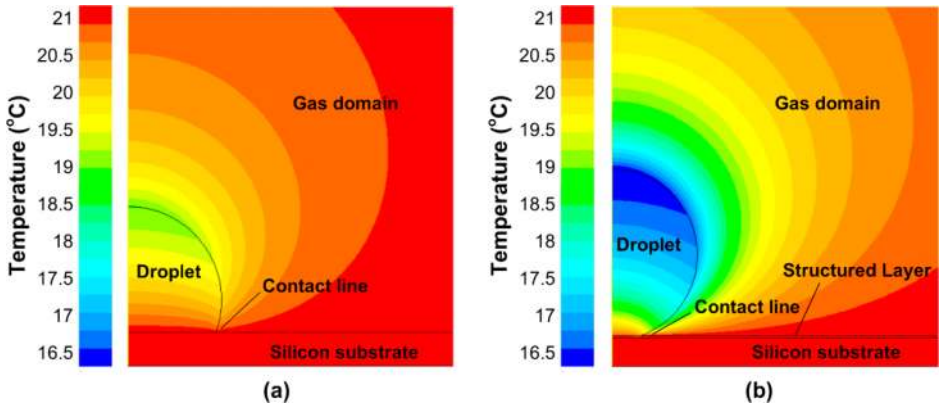

Figure 3. Temperature field in and around an evaporating 2 μL droplet resting on the (a) hydrophobic substrate (θ = 110°) and (b) superhydrophobic substrate (θ = 160°). The color legend on the left indicates the calculated temperature in °C.

5. RESULTS AND DISCUSSION

To first analyze and understand the quasi-steady transport details predicted by the present model, the case of a sessile droplet with 2 μL instantaneous volume is discussed in detail on both hydrophobic and superhydrophobic substrates in sections 5.1 and 5.2. In section 5.3, the influence of different transport mechanisms on the evaporation characteristics is quantitatively assessed. The instantaneous evaporation rates with decreasing droplet volume are predicted for droplets with 2 μL initial volume and are compared to experimental results[49] and a previous vapor diffusion-based model[13] in section 5.4.

5.1. Evaporative Cooling and Heat Transfer. The temperature distributions in and around a 2 μL droplet evaporating on hydrophobic and superhydrophobic substrates are shown in Figures 3a and 3b, respectively. Evaporation is observed to cool down the droplet interface significantly due to the local latent heat sink. The temperature gradients induced around the evaporating interface indicate the two primary paths of heat transfer to the interface: (1) heat transferred from the surrounding ambient gas and (2) heat supplied from the solid substrate through the liquid droplet. The temperature of the solid substrate, which acts as a high-conductivity lateral heat spreader, is nearly uniform.

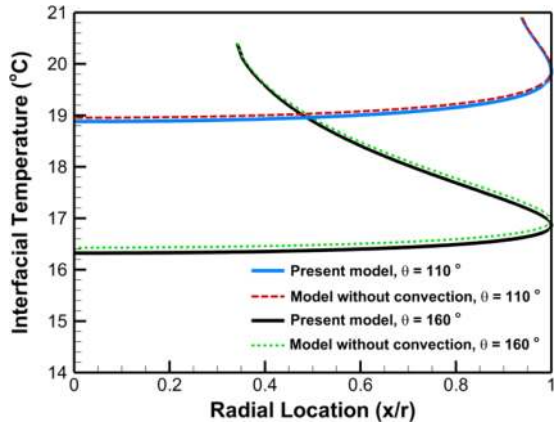

Figure 4. Temperature profiles along the droplet interfaces for both hydrophobic (θ = 110°) and superhydrophobic (θ = 160°) substrates (radial location is normalized by the droplet radius).

For the hydrophobic surface, 88.9% of the heat transferred to the interface is supplied from the substrate through the liquid droplet (the rest being supplied from the gas side of the interface); for the droplet on the superhydrophobic surface, on the other hand, the thermal resistance to heat flow by this path is increased due to the droplet geometry. For the larger contact angle (160° versus 110°), the ratio of the droplet height to its contact radius is increased (h/r_c = 5.67 versus 1.43) at constant droplet volume. Heat from the underlying substrate must travel a longer distance through a narrower droplet base area to arrive at the evaporating interface for the droplet on the superhydrophobic surface. As result, heat transferred through the liquid accounts for only 44.7% of the overall energy transferred to the interface for the droplet on the superhydrophobic surface.

A temperature difference of approximately 0.5 °C is seen across the structured layer at the contact line region. The influence of this layer in mitigating evaporation is found to be negligible (~1.2% reduction in the evaporation rate) since the structured layer has a similar thermal conductivity (k_{eff} = 0.54 W/(m K)) but a much smaller thickness (23 μm) compared to the water droplet.

The interfacial temperature profiles are plotted in Figure 4. The temperature drop along the evaporating interfaces is ~2 °C for the hydrophobic substrate and ~4 °C for the superhydrophobic substrate. This indicates that vapor diffusion-based models that assume isothermal conditions are not suitable, even for high thermal conductivity substrates that are not heated. The interfacial temperature increases slightly when the convective terms are absent from the model. The effects and importance of natural convection is discussed further in sections 5.2 and 5.3.

5.2. Vapor Diffusion and Natural Convection in Gas Domain. The vapor fraction contour maps in the gas domain surrounding the 2 μL droplet are shown in Figure 5. At the contact line region, the solid wall imposes geometric confinement and impedes diffusion of vapor evaporated from the contact line region into the open atmosphere. However, as indicated in Figures 3 and 4, the contact line region has the highest interfacial temperature and thus the highest local saturated vapor pressure (i.e., the highest vapor fraction, ρ_v/ρ_g). This highest local vapor pressure induces a vapor fraction gradient near the contact line region and drives vapor diffusion from the contact line to the open atmosphere. As a result, the local evaporation flux along the interface is highest at the contact line (see section 5.3).

Two prevailing mechanisms can induce natural convection in the gas phase: (1) an upward vapor concentration-dependent

dx.doi.org/10.1021/la4045286 | Langmuir 2013, 29, 15831−15841

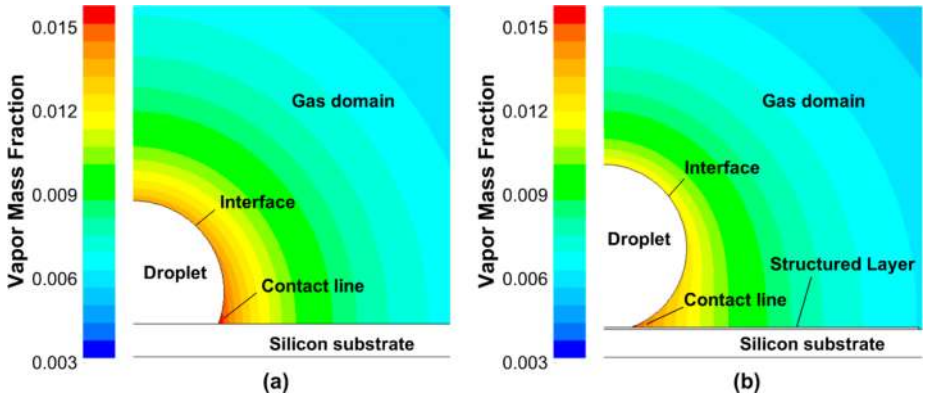

Figure 5. Vapor mass fraction near an evaporating 2 μL droplet on (a) the smooth hydrophobic substrate (θ = 110°) and (b) the structured superhydrophobic substrate (θ = 160°).

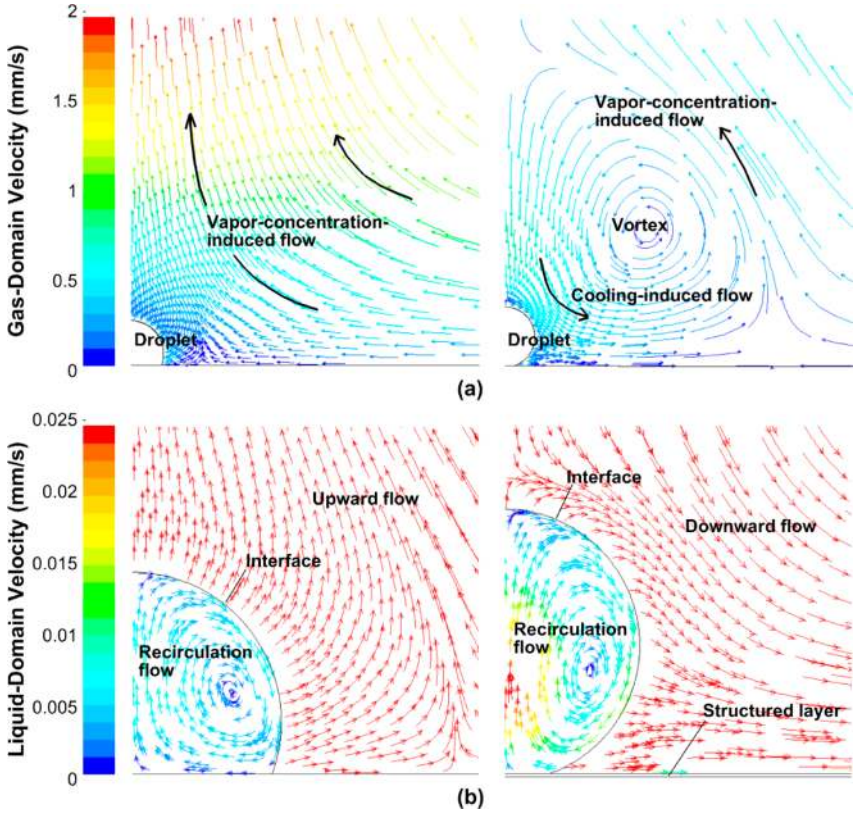

Figure 6. Natural convection velocity vectors in and around an evaporating 2 μL droplet (a) in the gas domain around the droplet (legend refers to velocities in the gas domain) and (b) within the droplet (legend refers to liquid velocities in the droplet) for the hydrophobic substrate (θ = 110°, left) and superhydrophobic substrate (θ = 160°, right).

buoyancy force due to the density difference between water vapor and air and (2) a downward thermal buoyancy force due to the evaporative cooling near the liquid–gas interface. The overall natural convection pattern is then governed by the balance of these two factors, as shown in Figure 6. For both substrates, the evaporative cooling effect near the interface weakens or reverses the vapor concentration-induced upward natural convection in the gas domain. For the hydrophobic substrate, the vapor concentration buoyancy force is stronger than the thermal buoyancy force, and net upward convection is observed throughout the gas domain. Conversely, for the superhydrophobic substrate, the temperature drop along the interface is strong enough to overcome the vapor buoyancy force and induces downward flow near the droplet interface. Further away from the droplet interface, the vapor buoyancy force again dominates and convection is upward. This creates a toroidal vortex in the gas domain above the droplet on a superhydrophobic surface.

Within the liquid phase of the droplets, a circulation flow is induced by the nonuniform temperature distribution (Figure 6b). At the center of the droplet, the warmer solid substrate causes an upward flow, while the cooler evaporating interface induces a downward flow along the periphery. The maximum velocity is 10 μm/s for the hydrophobic substrate and ~25 μm/s for the superhydrophobic substrate, corresponding to the driving liquid-phase temperature gradient. Convection in the liquid phase has negligible influence on droplet evaporation. Even though Marangoni convection is neglected in the model,

dx.doi.org/10.1021/la4045286 | *Langmuir* 2013, 29, 15831–15841

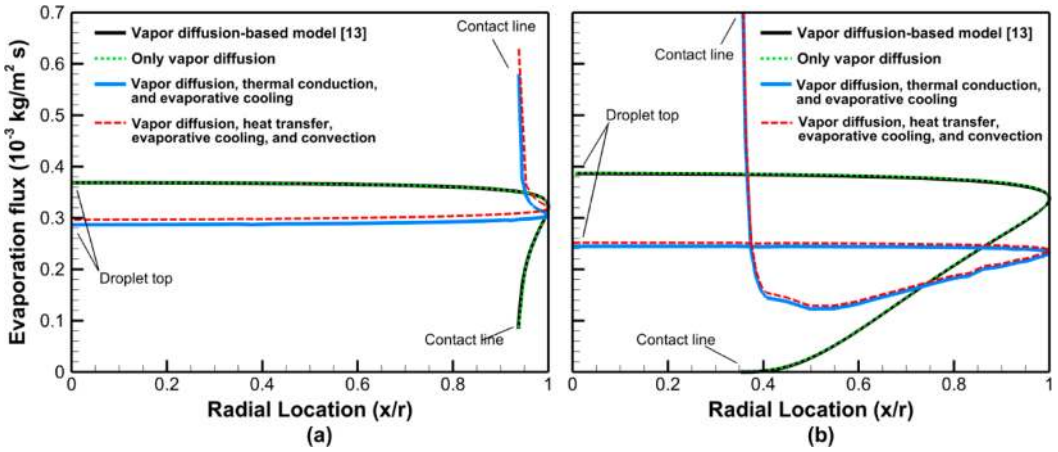

Figure 7. Local evaporation fluxes (radial location is normalized by the droplet radius) along the interface of the evaporating 2 μL droplet with different transport mechanisms included in the current model for (a) the hydrophobic substrate (θ = 110°) and (b) the superhydrophobic substrate (θ = 160°).

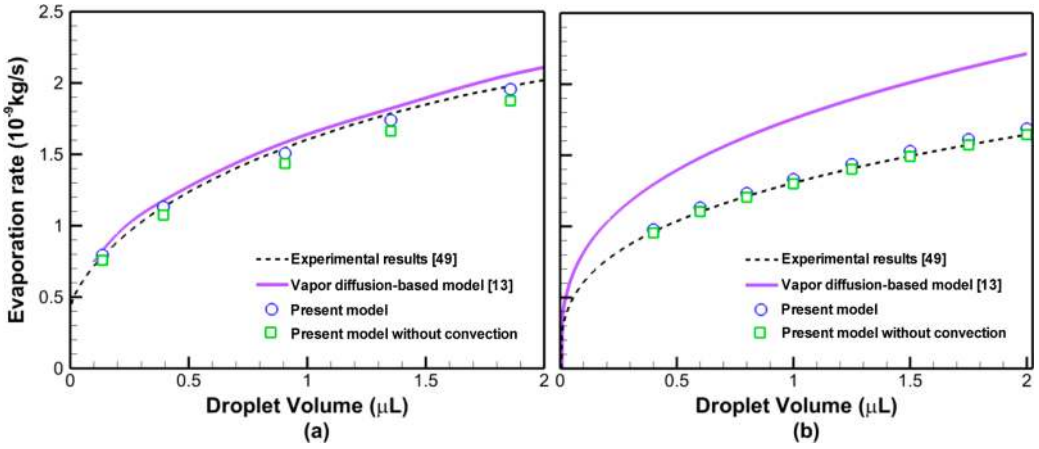

Figure 8. Evaporation rate as a function of evaporating droplet volume on (a) the hydrophobic substrate (to provide direct comparison to experimental data,[49] θ in the simulations is obtained from the experiments and varies from 115° to 95° as the droplet volume decreases from 1.86 to 0.14 μL) and (b) the superhydrophobic substrate (θ = 160° is constant from 2 to 0.4 μL).

its magnitude compared to natural convection in the liquid phase can be estimated by comparing the Marangoni and Rayleigh numbers for a 2 μL water droplet. With an experimentally observed Marangoni number that is 2 orders of magnitude smaller than the theoretical value for pure water,[5,26,33,54] Marangoni flow is expected to be weaker than liquid-phase natural convection in the droplet, which itself is shown to have a negligible effect on droplet evaporation in the present study.

5.3. Evaporation Flux and Influencing Factors. In addition to the total evaporation rate, the local evaporation flux along the droplet interface is investigated. The local evaporation flux along the droplet interface is plotted along the radial location on the droplet interface as shown in Figure 7, where the radial location is normalized by the droplet radius. Relevant heat and mass transfer mechanisms are sequentially incorporated into the numerical model and compared with the vapor diffusion-based model[13] to allow an assessment of the relative importance and impact of each different mechanism.

In multiple previous studies,[9−18] local evaporation flux was predicted by vapor diffusion-based models. When only vapor diffusion in the gas domain is considered, the numerically calculated local evaporation flux (green dashed line in Figure 7) agrees with Popov's vapor diffusion-based model[13] (black solid line in Figure 7) for both substrates and serves as validation with analytical theory. Under these conditions, the lowest evaporation flux of almost zero is observed at the contact line region, where the local geometry prevents vapor diffusion away from the interface to the open atmosphere.

The next case shown in Figure 7 (blue solid line) includes the evaporative cooling effect at the interface and conduction heat transfer in both fluid and solid phases; the local vapor pressure is coupled to the interfacial temperature. The local evaporation flux profiles are seen to be significantly altered by the inclusion of these mechanisms. As discussed in section 5.1, the temperature at the contact line is significantly larger than that at the top of the droplet, and thus the local vapor pressure is correspondingly higher. As a result, even if the gas domain geometry is not favorable to diffusion from the contact line region, the vapor pressure governs the high local evaporation flux at the corner region. This is observed for both hydrophobic and superhydrophobic surfaces. The highest evaporation flux at the corner region is ~1.2 g/(m^2 s) for the superhydrophobic surface.

A final case, which represents the comprehensive model, includes convection in the droplet and in the gas domain (red dashed line in Figure 7). For both substrates, since the vapor-buoyancy-driven upward natural convection in the gas phase is

dx.doi.org/10.1021/la4045286 | Langmuir 2013, 29, 15831−15841

weakened by the interface cooling effect (as discussed in section 5.2), its influence is less significant than observed on hydrophilic substrates in previous studies.[37,39] The weak upward gas-phase convection for the hydrophobic substrate (Figure 6a) slightly increases the local evaporation flux along the droplet interface (Figure 7a); this accounts for the corresponding interfacial temperature decrease observed in Figure 4 when convection is considered. For the superhydrophobic substrate, since upward convection is completely suppressed in the gas phase near the interface due to the stronger evaporative cooling effect, the influence of gas-phase convection in the model is found to be negligible (accounts for ∼2% increase in the evaporation rate).

It is emphasized that the local evaporation fluxes calculated by the present model deviate significantly from vapor diffusion-based models. Diffusion-only models do not consider the temperature gradient along the droplet interface and thereby do not capture the high evaporation flux near the contact line region.

5.4. Comparison to Experimental Evaporation Rates. In this section the instantaneous total evaporation rates calculated using the numerical model for an evaporating droplet with initial volume of 2 μL are compared against experimental results[49] and the vapor diffusion-based analytical model[13] under identical ambient conditions. It is noted that the numerical model assumes a quasi-steady state at each droplet volume. The contact angles employed for calculation of the evaporation rate correspond to the experimentally measured contact angles at each droplet volume. The contributions of the evaporative cooling and fluid convection effects to the overall evaporation rate are quantitatively determined. The evaporation rate is shown as a function of droplet volume in Figure 8. For the experimental cases, the evaporation rates are plotted from the experimental data for hydrophobic and superhydrophobic substrates.[49]

For the hydrophobic substrate (Figure 8a), both the vapor diffusion-based model and the present comprehensive model agree well with the experimental evaporation rates for the duration of evaporation; however, interrogation of the transport mechanisms that affect total evaporation rate in the sections above reveals that this close agreement is fortuitous and results from the neglect in the vapor diffusion model of two counteracting mechanisms (evaporative cooling and vapor-buoyancy-driven convection) of similar consequence at this contact angle. The present model, which includes all of the pertinent transport mechanisms for an evaporating water droplet, agrees to within 3% of the experimental results. The evaporative cooling effect, when assessed in isolation, suppresses the evaporation rate by ∼10%, while an accounting of the fluid convection enhances the evaporation rate by ∼4% from this baseline.

For the superhydrophobic substrate (Figure 8b), the vapor diffusion-based model[13] overestimates the evaporation rates by as much as ∼20% compared to the experimental results,[49] and the present model predicts the evaporation rates to within 2% of the experiments. The relative influence of the evaporative cooling considered in the comprehensive numerical model on the total evaporation rate is greater on the superhydrophobic surface than on the hydrophobic substrate (section 5.1). This strong evaporative cooling effect weakens the opposing mechanism of convection in the gas phase, and the deficiencies of vapor diffusion models are exposed at high contact angles. Compared to the vapor diffusion-based model,[13] the overall evaporation rate is reduced by ∼23.8% by evaporative cooling for the range of volumes investigated with the comprehensive numerical model developed in this work.

6. CONCLUSIONS

A comprehensive numerical model is developed to predict evaporation of sessile water droplets resting on unheated hydrophobic and superhydrophobic substrates. Evaporative cooling of the interface is accounted for, and vapor concentration is coupled to local temperature at the interface. Conjugate heat and mass transfer are solved in the solid substrate, liquid droplet, and surrounding gas. Buoyancy-driven convective flows in the droplet and vapor domains are also simulated.

When these effects are included, the local evaporation flux along the droplet interface is significantly altered from that predicted by a vapor diffusion-based model due to the evaporative cooling along the interface. At higher droplet contact angles, the thermal resistance between the solid substrate and the droplet interface increases. As a result, the temperature along the evaporating interface drops well below the ambient value, suppressing evaporation. This evaporative cooling effect decreases evaporation rates by ∼10% for the hydrophobic substrate and ∼23.8% for the superhydrophobic substrate compared to a model that only accounts for diffusion of vapor through the gas phase. Since the interfacial temperature (and local vapor pressure) is highest at the contact line region when evaporative cooling is accounted for, the maximum local evaporation flux is found at the contact line. Vapor diffusion-based models universally fail to predict these trends in the local evaporation flux.

The upward vapor buoyancy force due to the density difference between water vapor and air induces convection that acts to enhance evaporation. When convective effects are included in the model, it is found that the evaporation rate increases by ∼4% for the hydrophobic substrate and ∼2% for the superhydrophobic substrate compared to the cases that only consider evaporative cooling effects. The relative difference in enhancement between the surfaces is attributed to the stronger evaporative cooling in the case of the superhydrophobic surface, which acts to suppress the vapor-buoyancy-induced natural convection in the gas domain.

The numerically calculated total evaporation rates are compared to experimental data for evaporating droplets on hydrophobic and superhydrophobic substrates as a function of the quasi-static droplet volumes. Excellent agreement is shown; the calculated evaporation rates agree to within 3% for the hydrophobic substrate and 2% for the superhydrophobic substrate.

AUTHOR INFORMATION

Corresponding Author

*E-mail sureshg@purdue.edu (S.V.G.).

Notes

The authors declare no competing financial interest.

ACKNOWLEDGMENTS

Financial support for this work provided by the Cooling Technologies Research Center, a National Science Foundation Industry/University Cooperative Research Center at Purdue University, is gratefully acknowledged.

REFERENCES

(1) Kumari, N.; Garimella, S. V. Characterization of the heat transfer accompanying electrowetting or gravity-induced droplet motion. *Int. J. Heat Mass Transfer* **2011**, *54*, 4037−4050.

(2) Cheng, W.-L.; Han, F.-Y.; Liu, Q.-N.; Zhao, R.; Fan, H.-l. Experimental and theoretical investigation of surface temperature non-uniformity of spray cooling. *Energy* **2011**, *36*, 249−257.

(3) Singh, M.; Haverinen, H. M.; Dhagat, P.; Jabbour, G. E. Inkjet printing—process and its applications. *Adv. Mater.* **2010**, *22*, 673−685.

(4) Lim, T.; Han, S.; Chung, J.; Chung, J. T.; Ko, S.; Grigoropoulos, C. P. Experimental study on spreading and evaporation of inkjet printed pico-liter droplet on a heated substrate. *Int. J. Heat Mass Transfer* **2009**, *52*, 431−441.

(5) Marín, Á. G.; Gelderblom, H.; Lohse, D.; Snoeijer, J. H. Order-to-disorder transition in ring-shaped colloidal stains. *Phys. Rev. Lett.* **2011**, *107*, 085502.

(6) Zhang, S.; Li, Q.; Kinloch, I. A.; Windle, A. H. Ordering in a droplet of an aqueous suspension of single-wall carbon nanotubes on a solid substrate. *Langmuir* **2009**, *26*, 2107−2112.

(7) Carroll, N. J.; Rathod, S. B.; Derbins, E.; Mendez, S.; Weitz, D. A.; Petsev, D. N. Droplet-based microfluidics for emulsion and solvent evaporation synthesis of monodisperse mesoporous silica microspheres. *Langmuir* **2008**, *24*, 658−661.

(8) Chang, S. T.; Velev, O. D. Evaporation-induced particle microseparations inside droplets floating on a chip. *Langmuir* **2006**, *22*, 1459−1468.

(9) Picknett, R.; Bexon, R. The evaporation of sessile or pendant drops in still air. *J. Colloid Interface Sci.* **1977**, *61*, 336−350.

(10) Bourges-Monnier, C.; Shanahan, M. Influence of evaporation on contact angle. *Langmuir* **1995**, *11*, 2820−2829.

(11) Erbil, H. Y.; McHale, G.; Newton, M. Drop evaporation on solid surfaces: constant contact angle mode. *Langmuir* **2002**, *18*, 2636−2641.

(12) Hu, H.; Larson, R. G. Evaporation of a sessile droplet on a substrate. *J. Phys. Chem. B* **2002**, *106*, 1334−1344.

(13) Popov, Y. O. Evaporative deposition patterns: spatial dimensions of the deposit. *Phys. Rev. E* **2005**, *71*, 036313.

(14) Erbil, H. Y. Evaporation of pure liquid sessile and spherical suspended drops: A review. *Adv. Colloid Interface Sci.* **2012**, *170*, 67−86.

(15) Nguyen, T. A.; Nguyen, A. V. Increased evaporation kinetics of sessile droplets by using nanoparticles. *Langmuir* **2012**, *28*, 16725−16728.

(16) Nguyen, T. A.; Nguyen, A. V. On the lifetime of evaporating sessile droplets. *Langmuir* **2012**, *28*, 1924−1930.

(17) Song, H.; Lee, Y.; Jin, S.; Kim, H.-Y.; Yoo, J. Y. Prediction of sessile drop evaporation considering surface wettability. *Microelectron. Eng.* **2011**, *88*, 3249−3255.

(18) Yu, Y.-S.; Wang, Z.; Zhao, Y.-P. Experimental and theoretical investigations of evaporation of sessile water droplet on hydrophobic surfaces. *J. Colloid Interface Sci.* **2012**, *365*, 254−259.

(19) David, S.; Sefiane, K.; Tadrist, L. Experimental investigation of the effect of thermal properties of the substrate in the wetting and evaporation of sessile drops. *Colloids Surf., A* **2007**, *298*, 108−114.

(20) Dunn, G.; Wilson, S.; Duffy, B.; David, S.; Sefiane, K. The strong influence of substrate conductivity on droplet evaporation. *J. Fluid Mech.* **2009**, *623*, 329−351.

(21) Saada, M. A.; Chikh, S.; Tadrist, L. Evaporation of a sessile drop with pinned or receding contact line on a substrate with different thermophysical properties. *Int. J. Heat Mass Transfer* **2013**, *58*, 197−208.

(22) Lopes, M. C.; Bonaccurso, E.; Gambaryan-Roisman, T.; Stephan, P. Influence of the substrate thermal properties on sessile droplet evaporation: Effect of transient heat transport. *Colloids Surf., A* **2013**, in press.

(23) Talbot, E.; Berson, A.; Brown, P.; Bain, C. Evaporation of picoliter droplets on surfaces with a range of wettabilities and thermal conductivities. *Phys. Rev. E* **2012**, *85*, 061604.

(24) Deegan, R. D.; Bakajin, O.; Dupont, T. F.; Huber, G.; Nagel, S. R.; Witten, T. A. Contact line deposits in an evaporating drop. *Phys. Rev. E* **2000**, *62*, 756.

(25) Hu, H.; Larson, R. G. Analysis of the effects of Marangoni stresses on the microflow in an evaporating sessile droplet. *Langmuir* **2005**, *21*, 3972−3980.

(26) Hu, H.; Larson, R. G. Marangoni effect reverses coffee-ring depositions. *J. Phys. Chem. B* **2006**, *110*, 7090−7094.

(27) Ristenpart, W.; Kim, P.; Domingues, C.; Wan, J.; Stone, H. Influence of substrate conductivity on circulation reversal in evaporating drops. *Phys. Rev. Lett.* **2007**, *99*, 234502.

(28) Xu, X.; Luo, J.; Guo, D. Criterion for reversal of thermal Marangoni flow in drying drops. *Langmuir* **2009**, *26*, 1918−1922.

(29) Bhardwaj, R.; Fang, X.; Attinger, D. Pattern formation during the evaporation of a colloidal nanoliter drop: a numerical and experimental study. *New J. Phys.* **2009**, *11*, 075020.

(30) Karapetsas, G.; Matar, O. K.; Valluri, P.; Sefiane, K. Convective rolls and hydrothermal waves in evaporating sessile drops. *Langmuir* **2012**, *28*, 11433−11439.

(31) Sefiane, K.; Moffat, J.; Matar, O.; Craster, R. Self-excited hydrothermal waves in evaporating sessile drops. *Appl. Phys. Lett.* **2008**, *93*, 074103−074103−3.

(32) Pan, Z.; Wang, F.; Wang, H. Instability of Marangoni toroidal convection in a microchannel and its relevance with the flowing direction. *Microfluid. Nanofluid.* **2011**, *11*, 327−338.

(33) Dhavaleswarapu, H. K.; Migliaccio, C. P.; Garimella, S. V.; Murthy, J. Y. Experimental investigation of evaporation from low-contact-angle sessile droplets. *Langmuir* **2009**, *26*, 880−888.

(34) Girard, F.; Antoni, M.; Sefiane, K. On the effect of Marangoni flow on evaporation rates of heated water drops. *Langmuir* **2008**, *24*, 9207−9210.

(35) Dhavaleswarapu, H. K.; Murthy, J. Y.; Garimella, S. V. Numerical investigation of an evaporating meniscus in a channel. *Int. J. Heat Mass Transfer* **2012**, *55*, 915−924.

(36) Wang, H.; Pan, Z.; Garimella, S. V. Numerical investigation of heat and mass transfer from an evaporating meniscus in a heated open groove. *Int. J. Heat Mass Transfer* **2011**, *54*, 3015−3023.

(37) Saada, M. A.; Chikh, S.; Tadrist, L. Numerical investigation of heat and mass transfer of an evaporating sessile drop on a horizontal surface. *Phys. Fluids* **2010**, *22*, 112115.

(38) Kelly-Zion, P.; Pursell, C.; Vaidya, S.; Batra, J. Evaporation of sessile drops under combined diffusion and natural convection. *Colloids Surf., A* **2011**, *381*, 31−36.

(39) Carle, F.; Sobac, B.; Brutin, D. Experimental evidence of the atmospheric convective transport contribution to sessile droplet evaporation. *Appl. Phys. Lett.* **2013**, *102*, 061603.

(40) Sobac, B.; Brutin, D. Thermal effects of the substrate on water droplet evaporation. *Phys. Rev. E* **2012**, *86*, 021602.

(41) Kelly-Zion, P.; Pursell, C. J.; Hasbamrer, N.; Cardozo, B.; Gaughan, K.; Nickels, K. Vapor distribution above an evaporating sessile drop. *Int. J. Heat Mass Transfer* **2013**, *65*, 165−172.

(42) Jönsson-Niedziółka, M.; Lapierre, F.; Coffinier, Y.; Parry, S.; Zoueshtiagh, F.; Foat, T.; Thomy, V.; Boukherroub, R. EWOD driven cleaning of bioparticles on hydrophobic and superhydrophobic surfaces. *Lab Chip* **2011**, *11*, 490−496.

(43) Angelis, F. D.; Gentile, F.; Mecarini, F.; Das, G.; Moretti, M.; Candeloro, P.; Coluccio, M.; Cojoc, G.; Accardo, A.; Liberale, C. Breaking the diffusion limit with super-hydrophobic delivery of molecules to plasmonic nanofocusing SERS structures. *Nat. Photonics* **2011**, *5*, 682−687.

(44) Ebrahimi, A.; Dak, P.; Salm, E.; Dash, S.; Garimella, S. V.; Bashir, R.; Alam, M. A. Nanotextured superhydrophobic electrodes enable detection of attomolar-scale DNA concentration within a droplet by non-faradaic impedance spectroscopy. *Lab Chip* **2013**, in press.

(45) McHale, G.; Aqil, S.; Shirtcliffe, N.; Newton, M.; Erbil, H. Analysis of droplet evaporation on a superhydrophobic surface. *Langmuir* **2005**, *21*, 11053−11060.

(46) Dash, S.; Kumari, N.; Garimella, S. Characterization of ultrahydrophobic hierarchical surfaces fabricated using a single-step fabrication methodology. *J. Micromech. Microeng.* **2011**, *21*, 105012.
(47) Shin, D. H.; Lee, S. H.; Jung, J.-Y.; Yoo, J. Y. Evaporating characteristics of sessile droplet on hydrophobic and hydrophilic surfaces. *Microelectron. Eng.* **2009**, *86*, 1350−1353.
(48) Gelderblom, H.; Marin, A. G.; Nair, H.; van Houselt, A.; Lefferts, L.; Snoeijer, J. H.; Lohse, D. How water droplets evaporate on a superhydrophobic substrate. *Phys. Rev. E* **2011**, *83*, 026306.
(49) Dash, S.; Garimella, S. V. Droplet evaporation dynamics on a superhydrophobic surface with negligible hysteresis. *Langmuir* **2013**, *29*, 10785−10795.
(50) Pan, Z.; Wang, H. Bénard−Marangoni instability on evaporating menisci in capillary channels. *Int. J. Heat Mass Transfer* **2013**, *63*, 239−248.
(51) Semenov, S.; Starov, V. M.; Rubio, R. G.; Velarde, M. G. Computer simulations of evaporation of pinned sessile droplets: influence of kinetic effects. *Langmuir* **2012**, *28*, 15203−15211.
(52) Pan, Z.; Wang, H. Symmetry-to-asymmetry transition of Marangoni flow at a convex volatizing meniscus. *Microfluid. Nanofluid.* **2010**, *9*, 657−669.
(53) Wang, H.; Murthy, J. Y.; Garimella, S. V. Transport from a volatile meniscus inside an open microtube. *Int. J. Heat Mass Transfer* **2008**, *51*, 3007−3017.
(54) Gelderblom, H.; Bloemen, O.; Snoeijer, J. H. Stokes flow near the contact line of an evaporating drop. *J. Fluid Mech.* **2012**, *709*, 69−84.
(55) Mathur, S.; Murthy, J. A pressure-based method for unstructured meshes. *Num. Heat Transfer* **1997**, *31*, 195−215.
(56) Fluent, *ANSYS FLUENT 14.0: User's Guide*, ANSYS-Fluent Inc.: Lebanon, NH, 2009.